Supplementary Information

Tailoring Polarization in WSe_2 Quantum Emitters through Deterministic Strain Engineering

Athanasios Paralikis,[1] Claudia Piccinini,[1] Abdulmalik A. Madigawa,[1] Pietro Metuh,[1] Luca Vannucci,[1] Niels Gregersen,[1] and Battulga Munkhbat[1,†]

[1] *Department of Electrical and Photonics Engineering, Technical University of Denmark, 2800 Kongens Lyngby, Denmark*

[†]E-mail: bamunk@dtu.dk

Contents

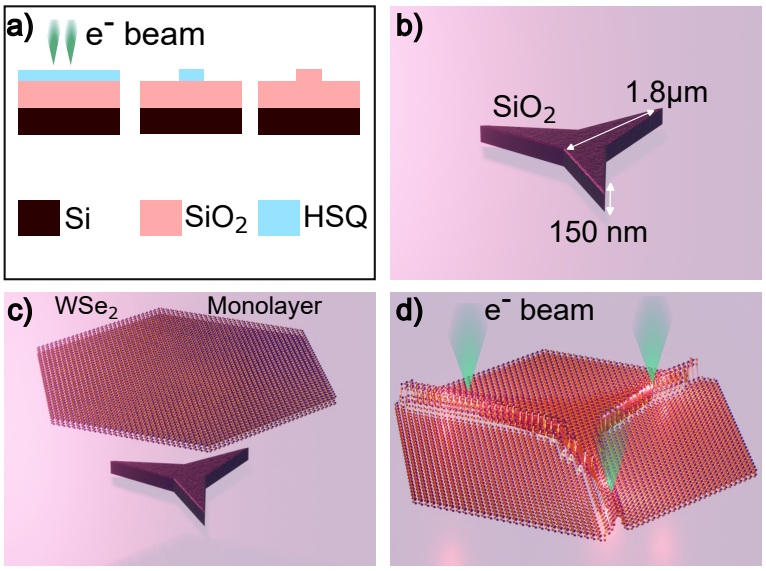

Supplementary Figure 1: (a) Schematic representation of substrate fabrication process. The resist is spin-coated on the substrate and illuminated with an electron beam. Later on, it is developed to reveal the final pattern. It is well documented that the chemical composition of the HSQ resist changes into SiO_2. **(b)** Illustration of a three-pointed star nanostructure, with an apex-to-base ratio = 1.8 µm and height of 150 nm. **(c)** Depiction of the dry transfer method. The monolayer is on top of PDMS, which is attached to a microscope slide. **(d)** Post-transfer irradiation process for the deterministic introduction of defects in the lattice.

Supplementary Note 1: Sample fabrication and characterization procedures. Supplementary Figure 1 presents the entire fabrication process of a sample. For the host chip, the nanostructures are fabricated on a Si/SiO_2 substrate (see Methods). For the three-pointed star, the apex-to-base distance measures 1.8 µm, and the height ranges between 140-150 nm, with the other designs having similar ratios. Preliminary results suggest that a height lower than ∼140 nm could not efficiently host quantum emitters due to the inadequate mechanical strain applied on the monolayer. On the other hand, taller structures (∼200 nm) negatively affect the transferring process, damage the flakes, and create bubbles that negatively affect the formation of nanowrinkles.

Once the chip is fabricated, we exfoliate the monolayer on PDMS situated on a glass slide using the standard scotch tape method.[1] The monolayers are identified through their RT PL emission spectra using a confocal microscope setup. Subsequently, the flakes are deposited on the patterned chips using a deterministic approach to the standard dry-transfer technique with the help of a transfer stage. To get a clear view of the samples' morphology, their AFM and SEM images are acquired.
Finally, the samples are irradiated with an electron beam (see Methods) to introduce defects in the lattice, specifically targeting the nanowrinkles. Subsequently, the sample is introduced into the cryostat for optical characterization.

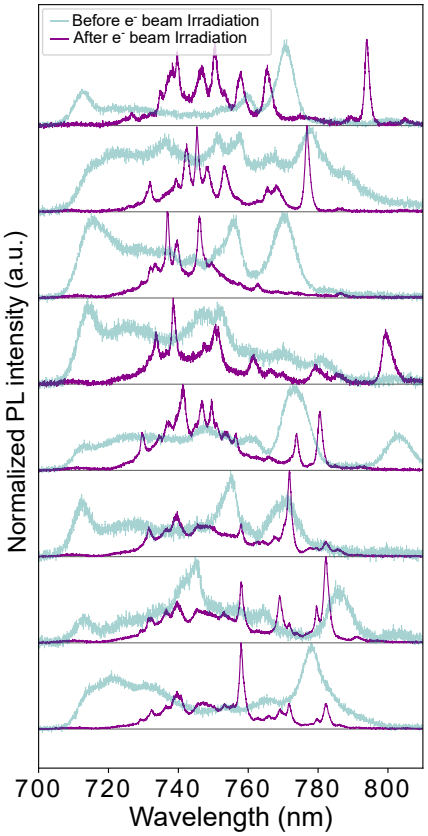

Supplementary Figure 2: PL spectra of areas under mechanical strain before and after EBL Irradiation for the deterministic introduction of defects in the crystal lattice.

Supplementary Note 2: The importance of defect engineering. The importance of defects in fabricating SPEs in TMDs has been controversial. Nuances in the fabrication process do not allow for pristine layers without natural defects, so the experimental data are difficult to interpret. Despite that, some works have attempted to theoretically explore the influence of both strain and defect engineering in TMDs. [2, 3, 4, 5] The main takeaway from this literature is that both strain and defect engineering are necessary for the confinement of charge carriers and their efficient recombination for the production of single photons. While applying strain alters the bands to form weakly localized excitons by funneling free carriers to the strained areas, their bright recombination would be spin - or valley - prohibited [2]. Hence, if the energy of the highly localized defect states is close to the bands, they can hybridize, allowing for the bright recombination of the charge carriers. [2, 4] Therefore, a combination of strain and defect engineering is paramount for efficiently fabricating SPEs in TMD monolayers. In their work regarding SPEs in monolayer WSe_2, Xu D. et al.[3] observe that unstrained regions do not exhibit localized emission lines whether or not they are irradiated with an e-beam. In our samples, even weakly strained regions show the same behavior. In contrast, strained regions irradiated by an e-beam host several well-isolated and defined novel emission lines. These findings perfectly agree with the results presented in Supplementary Figure 2, where the PL spectra of eight exemplary strained regions are given both before (teal lines) and after (magenta lines) the deterministic introduction of defects in the lattice. Despite defect-engineering not being a regular practice in literature [6, 7, 8, 9, 10, 11], the data presented in Supplementary Figure 2 combined with some previous work[4, 3, 5, 2], present enough reasoning for us to adopt defect-engineering as a consistent part of our fabrication process. Thus, every sample presented in this work has been irradiated with an e-beam to deterministically introduce defects to the lattice. Details on the dosage can be found in the Method section.

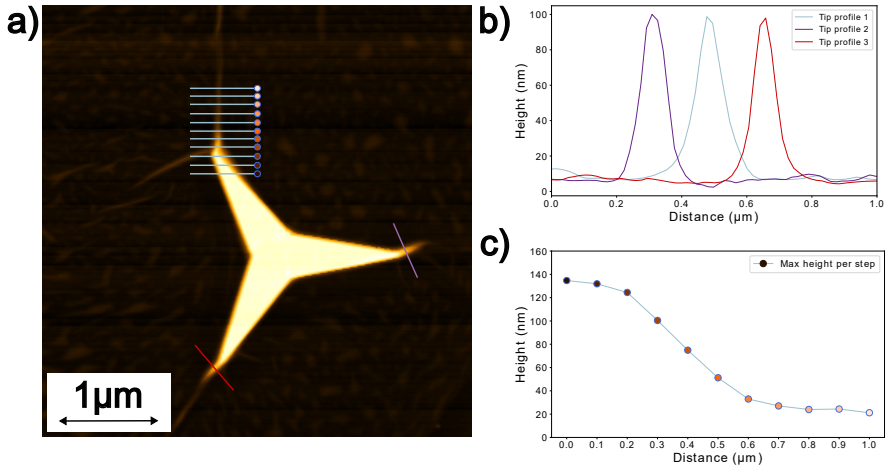

Supplementary Figure 3: **(a)** AFM image of an exemplary three-pointed star structure with monolayer WSe_2. The color-coded lines and bullets represent the areas of data collection for the following graphs. **(b)** Morphological profile comparison between the wrinkles formed on the three different tips. The data are collected from a relatively similar distance from the vertices' tips, and the resulting profiles are color-coded according to the collection sites in (a) for improved readability. We notice the similarity between the profiles in terms of height and width. **(c)** Extended morphological profile of a single wrinkle (Tip profile 1). The profile is measured in 0.1 µm increments, starting from the vertex (see color-coded bullet points). A relatively steep decline can be observed, with the formed wrinkle's height stabilizing after approximately 0.5 µm.

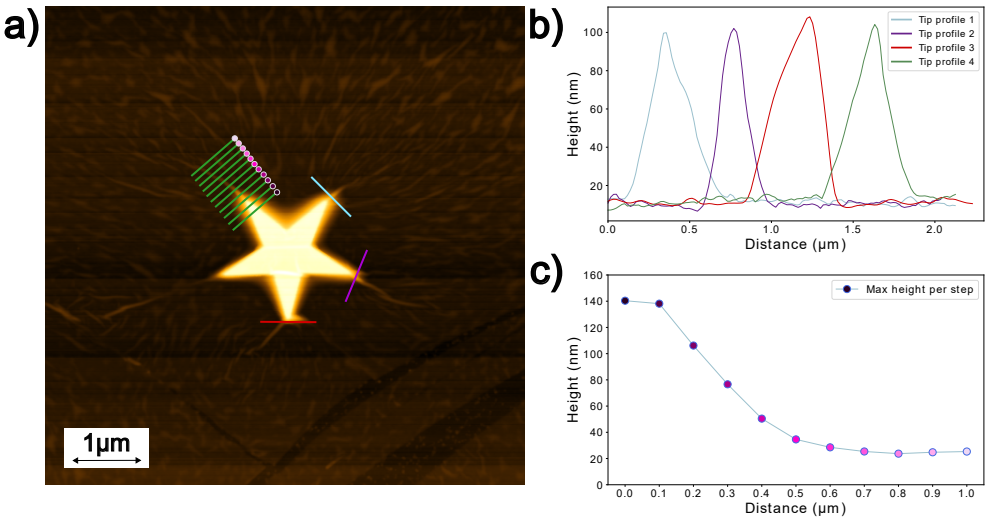

Supplementary Figure 4: **(a)** AFM image of an exemplary five-pointed star structure with monolayer WSe_2. The color-coded lines and bullets represent the areas of data collection for the following graphs. **b)** Morphological profile comparison between the wrinkles formed on the two different tips. The data are collected from a relatively similar distance from the vertices' tips, and the resulting profiles are color-coded according to the collection sites in (a) for improved readability. **(c)** Extended morphological profile of the wrinkle connecting the triangles. The profile is measured in 0.1 µm increments, extended to the vertices themselves (see color-coded bullet points). A relatively steep decline can observed in both tips, with the height of the formed wrinkle stabilizing after approximately 0.3 µm.

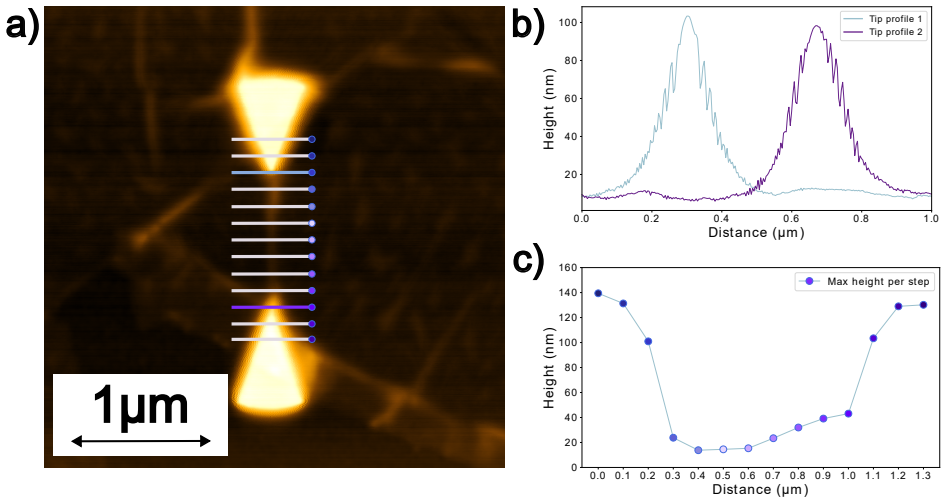

Supplementary Figure 5: **(a)** AFM image of an exemplary bowtie structure with monolayer WSe_2. The color-coded lines and bullets represent the areas of data collection for the following graphs. **(b)** Morphological profile comparison between the wrinkles formed on the four different tips. The fifth vertex was omitted as it did not host any visible wrinkle or quantum emitter. The data are collected from a relatively similar distance from the vertices' tips, and the resulting profiles are color-coded according to the collection sites in (a) for improved readability. **(c)** Extended morphological profile of a single wrinkle (Tip profile 4). The profile is measured in 0.1 μm increments, starting from the vertex (see color-coded bullet points). A relatively steep decline can be observed, with the height of the formed wrinkle stabilizing after approximately 0.5 μm.

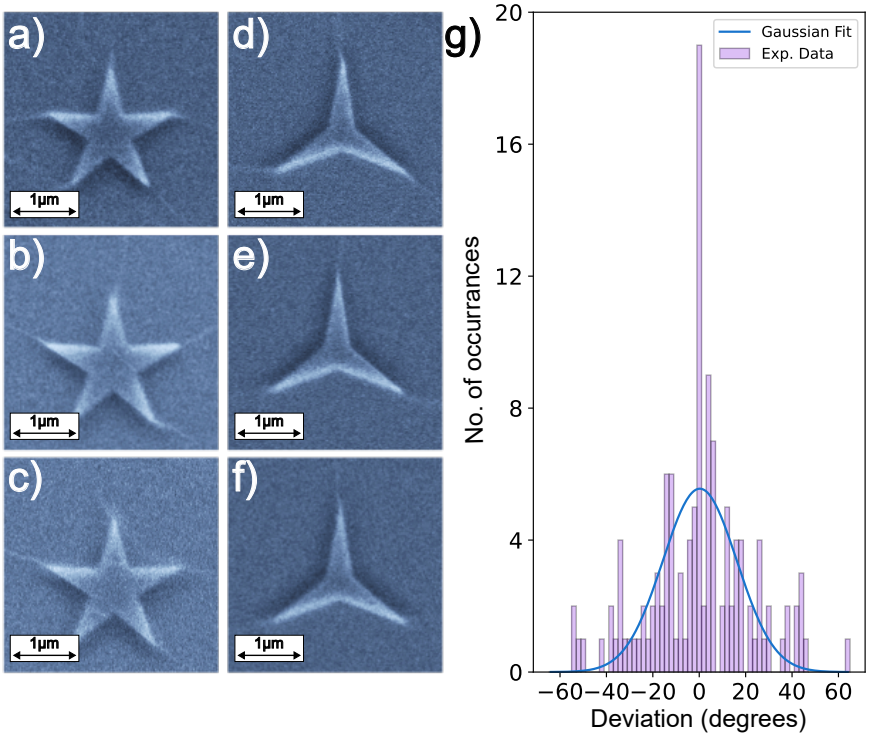

Supplementary Figure 6: (a-f) SEM images of WSe_2 monolayer flakes on top exemplary of star-like structures with wrinkles forming on the tips of their vertices. Images a-c depict 5-point structures, while images d-f depict 3-point structures. We notice the wrinkles formed on the vertices of the stars, which host the quantum emitters discussed in the main text. **(g)** Statistical analysis of the misalignment of directionality between the vertices of the stars and the wrinkles created on their tips (deviation) versus the number of occurrences of said deviation in all usable structures. The deviation is given in degrees, with the middle point of the axis (0°) signaling that the vertices and wrinkles are completely aligned. Positive (negative) degree values signal that the wrinkle deviates to the vertex's right (left) side. The performance of the structures is evaluated through the characteristics of a Gaussian distribution. With the mean value of the distribution (x_0) at $0.25° \pm 2.55°$ and the standard deviation (2σ) at $16.0° \pm 2.5°$, it is safe to conclude that these structures provide an adequate amount of strain - and subsequent polarization - control.

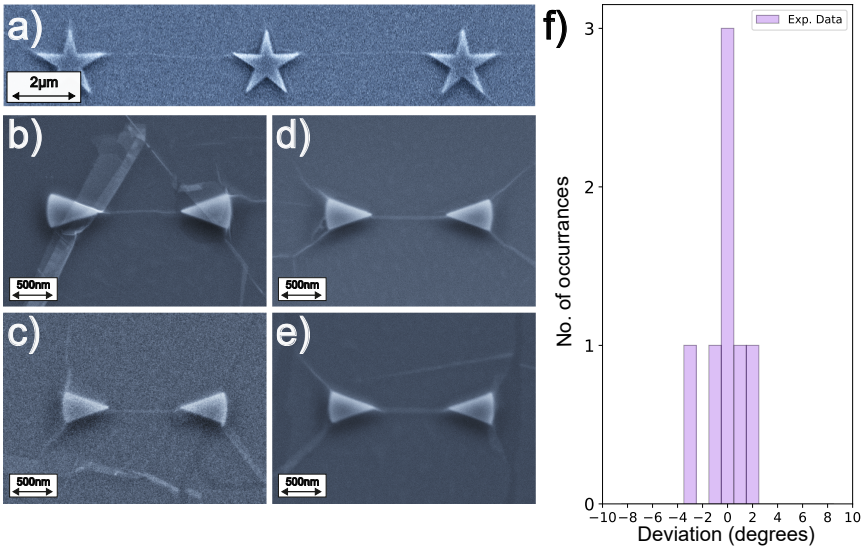

Supplementary Figure 7: **(a)** SEM image of 5-pointed star structures with a connecting wrinkle through their vertices. **(b-e)** SEM images of WSe_2 monolayer flakes on top of bowtie structures with wrinkles forming on the tips of their vertices facing each other. Some wrinkles form on the bases of the isosceles triangles comprising the bowtie, but they are of no serious concern, as the wrinkle connecting the structures is well isolated. **(e)** Histogram of the misalignment of directionality between the axis connecting the vertices of the triangles and the wrinkles created on their tips (deviation) versus the number of occurrences of said deviation in all usable structures.

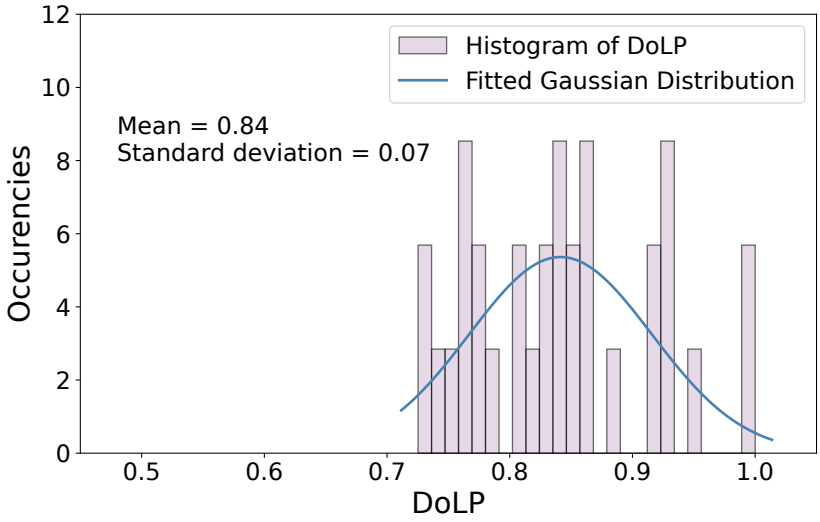

Supplementary Figure 8: Histogram showing the distribution of Degree of Linear Polarization (DoLP) values for quantum emitters. The x-axis represents DoLP values, while the y-axis indicates the frequency of occurrences. The overlaid Gaussian distribution reveals an average DoLP value of 0.84 with a standard deviation of 0.07.

Supplementary Note 3: Different excitation schemes. The excitation scheme can drastically alter the features of an emission spectrum. Especially in the case of the CW LED used in Figures 1-4, the excitation introduces thermal fluctuation leading to a noticeable redshift [12, 4] of the emission line. Furthermore, it introduces photo-excited free carriers that lead to severe charge noise around the emitter, resulting in homogeneous emission line broadening. To visualize the effect of the different excitation schemes, we measured PL spectra under CW LED at 470 nm and 532 nm pulsed laser from the same emitter. Supplementary Figure 9 presents the two spectra where we notice that the one attributed to pulsed excitation (blue curve) is

narrower while attaining a characteristic Lorentzian shape. Here, we also notice the phonon sideband discussed in Figure 5 of the main text. On the other hand, the spectrum attributed to LED excitation (purple curve) has a Gaussian shape, which is distinctive of the homogeneous broadening that has affected the emission line.

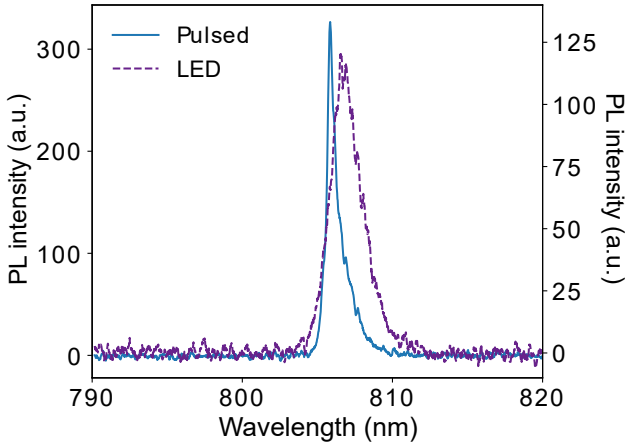

Supplementary Figure 9: PL spectra at T = 4 K from the same quantum emitter under two different excitation schemes. The blue curve (left y-axis) is collected under excitation by an 80 MHz pulsed laser at 532 nm, while the purple dashed curve (right y-axis) is collected under excitation by an LED at 470 nm.

Supplementary Note 4: Lifetime dynamics. In Figure 5b, we presented the time-resolved PL (TRPL) measurement of the exemplary SPE. The plot reveals two distinct decays fitted with two exponential functions to extract the corresponding decay rates. The slow decay ($\tau_{\text{slow}} = 13.3 \pm 0.2$ ns) is the one making the greatest contribution to the curve ($\sim 94\%$), and its range agrees with the reported lifetime of SPEs in monolayer WSe_2 [6, 9, 13, 14, 8, 15, 16]. What is more intriguing is the initial fast decay ($\tau_{\text{fast}} = 0.16 \pm 0.24$ ns) that seems to originate from some unidentified rapid process limited by the instrument response function (IRF), which arises from the resolution limit of the time tagger and is typically around 150 ps. One possible cause of origin for the τ_{fast} is that the SNSPDs capture some weak leakage from the excitation laser. However, we rule this case out since the detection efficiency of our SNSPDs (optimized above 700 nm) is relatively poor at λ= 532 nm. Another likely scenario involves detecting a faint signal from the extended emissions of the delocalized exciton and charged excitons in the planar monolayer around the WSe_2 SPE. To verify this speculation, we performed an additional lifetime measurement of the delocalized exciton from the planar monolayer WSe_2 at 730 nm shown in Supplementary Figure 10a, which typically has a lifetime of around 120 ps [17]. Indeed, Supplementary Figure 10b presents the comparison between the two TRPL measurements. The fitting reveals a lifetime of 0.18 ± 0.06 nm for the delocalized exciton, which is relatively similar to τ_{fast}. This result makes the weak leakage of the delocalized exciton the most probable cause of the fast decay. Lastly, τ_{fast} could be associated with an unidentified process of the localized defect states. However, this requires further investigation, which falls beyond the scope of this paper.

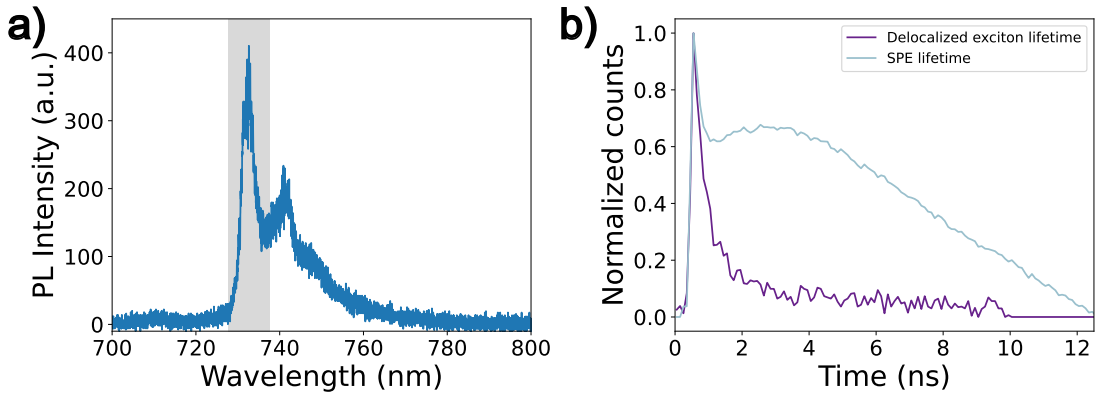

Supplementary Figure 10: (a) PL spectrum (4K) taken from a pristine monolayer area of WSe_2 under above band excitation of 532 nm femtosecond pulsed laser (80 MHz). The grey area highlights the spectral region around the A exciton emission, which is later spectrally isolated via a band pass filter to acquire the lifetime measurement presented in (b). (b) Time-resolved photoluminescence (TRPL) measurements of the delocalized A exciton (purple) and the SPE (blue), investigated in Figure 5 of the main text. Since the reported lifetime of the A exciton [17] is below the bottleneck of our setup, the purple curve acts as the IRF. An exponential fitting function reveals an IRF of $0.18 \pm 0.06nm$, while the fitting of the fast decay in the SPE lifetime gives a value of $0.16 \pm 0.24nm$. The resemblance hints at a correlation between the two dynamic processes.

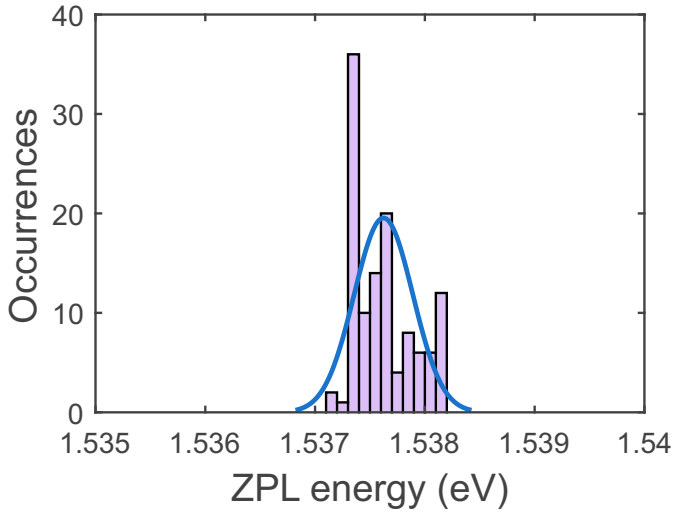

Supplementary Figure 11: Histogram of the spectral jittering of the exemplary emitter presented in Figure 5, with a bin width of 0.1 meV. The Gaussian fitting reveals an average central position of the peak at 1.5365 eV with a standard deviation of 0.267 meV.

Supplementary Note 5: Alternative materials for the nanopillars. The considerably high dose needed to cure HSQ-based resist and its short shelf life led to the investigation of other e-beam resists. We fabricated 200 nm-thick nanopillars with the same structure as the ones in this work with the highly sensitive AR-N 7520.11, which was spin-coated at 4000 rpm (1000 rpm/s, 60 s) after depositing HMDS for promoting its adhesion on the SiO_2 substrate. The sample was soft baked on a hotplate at 85 °C for 1 min and patterned with an e-beam writer (Raith eLINE, 30 kV, 60 µC/cm^2, 15 µm aperture). The resist was then developed in AR 300-47 for 50 s, followed by a 60 s rinse in water. Supplementary Figure 12 shows an AFM image of a three-pointed star nanopillar after the transfer of a WSe_2.

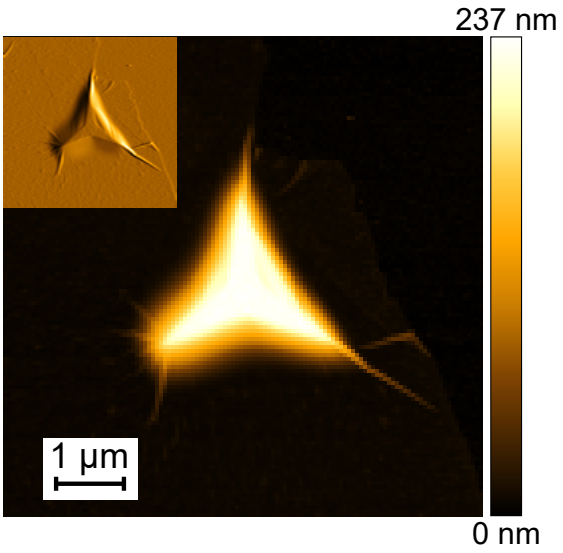

Supplementary Figure 12: AFM image of a WSe_2 flake on 200 nm-thick AR-N 7520.11 nanopillars and its false-shading representation (inset).

References

[1] Castellanos-Gomez, A. *et al.* Deterministic transfer of two-dimensional materials by all-dry viscoelastic stamping. *2D Materials* **1**, 011002 (2014).

[2] Linhart, L. *et al.* Localized Intervalley Defect Excitons as Single-Photon Emitters in WSe2. *Physical Review Letters* **123** (2019).

[3] Xu, D. D. *et al.* Conversion of classical light emission from a nanoparticle-strained wse2 monolayer into quantum light emission via electron beam irradiation. *Advanced Materials* **35**, 2208066 (2023).

[4] Parto, K., Azzam, S. I., Banerjee, K. & Moody, G. Defect and strain engineering of monolayer WSe2 enables site-controlled single-photon emission up to 150 K. *Nature Communications* **12** (2021).

[5] Montblanch, A. R., Barbone, M., Aharonovich, I., Atatüre, M. & Ferrari, A. C. Layered materials as a platform for quantum technologies. *Nature Nanotechnology 2023 18:6* **18**, 555–571 (2023).

[6] Kumar, S., Kaczmarczyk, A. & Gerardot, B. D. Strain-Induced Spatial and Spectral Isolation of Quantum Emitters in Mono- and Bilayer WSe2. *Nano Letters* **15**, 7567–7573 (2015).

[7] Palacios-Berraquero, C. *et al.* Large-scale quantum-emitter arrays in atomically thin semiconductors. *Nature Communications* **8** (2017).

[8] Branny, A., Kumar, S., Proux, R. & Gerardot, B. D. Deterministic strain-induced arrays of quantum emitters in a two-dimensional semiconductor. *Nature Communications* **8** (2017).

[9] Tripathi, L. N. *et al.* Spontaneous emission enhancement in strain-induced wse2 monolayer-based quantum light sources on metallic surfaces. *ACS photonics* **5**, 1919–1926 (2018).

[10] Luo, Y. *et al.* Deterministic coupling of site-controlled quantum emitters in monolayer WSe2 to plasmonic nanocavities (2018).

[11] Kim, H., Moon, J. S., Noh, G., Lee, J. & Kim, J.-H. Position and frequency control of strain-induced quantum emitters in wse2 monolayers. *Nano letters* **19**, 7534–7539 (2019).

[12] von Helversen, M. *et al.* Temperature dependent temporal coherence of metallic-nanoparticle-induced single-photon emitters in a WSe ₂ monolayer. *2D Materials* **10**, 045034 (2023).

[13] So, J. P. *et al.* Polarization Control of Deterministic Single-Photon Emitters in Monolayer WSe2. *Nano Letters* **21**, 1546–1554 (2021).

[14] Iff, O. *et al.* Purcell-Enhanced Single Photon Source Based on a Deterministically Placed WSe2Monolayer Quantum Dot in a Circular Bragg Grating Cavity. *Nano Letters* **21**, 4715–4720 (2021).

[15] He, Y.-M. *et al.* Single quantum emitters in monolayer semiconductors. *Nature nanotechnology* **10**, 497–502 (2015).

[16] Srivastava, A. *et al.* Optically active quantum dots in monolayer wse2. *Nature nanotechnology* **10**, 491–496 (2015).

[17] Liu, Y., Li, H., Qiu, C., Hu, X. & Liu, D. Layer-dependent signatures for exciton dynamics in monolayer and multilayer wse 2 revealed by fluorescence lifetime imaging measurement. *Nano Research* **13**, 661–666 (2020).